INTERNATIONAL JOURNAL FOR NUMERICAL METHODS IN FLUIDS, VOL. 25, 1185–1205 (1997)

NORMAL FLOW BOUNDARY CONDITIONS IN 3D CIRCULATION MODELS

DANIEL R. LYNCH* AND MONICA J. HOLBOKE

Dartmouth College, Hanover, NH, U.S.A.

SUMMARY

The problem of enforcing normal transport conditions on 3D velocity fields is considered in the context of 'wave equation' finite element models. A procedure for strong enforcement of the transport constraint is given. The procedure is identical for Neumann (transport known) and Dirichlet (pressure known) problems, which are treated reversibly. All local mass and force balance relations are retained in the FEM system. A global mass conservation property is proven for the general 3D, discrete-time case. Examples demonstrate the quality of the solutions and the practicality of the approach.© 1997 John Wiley & Sons, Ltd.

Int. J. Numer. Meth. Fluids, **25**: 1185–1205 (1997).

No. of Figures: 24. No. of Tables: 0. No. of References: 22.

1. INTRODUCTION

Use of the finite element method for estuarine and coastal circulation studies has grown significantly in recent years. Practical 3D problems are now being solved on large, unstructured meshes using both harmonic-in-time and more general time-stepping approaches. The combination of advanced turbulence closure, tidal time resolution and variable spatial resolution (both horizontally and vertically) provides a new, comprehensive simulation capability for these important environmental systems. (For recent reviews see References 1 and 2. References 3 and 4 provide state-of-the-art collections.)

As in other areas of fluid mechanics, boundary conditions continue to be a focus of concern, even for 2D problems. Recent BC contributions in the FEM coastal context include those of Westerink *et al.*,[5] who examined the role of BCs in the generation of spurious modes, Johnsen and Lynch,[6,7] who developed radiation BCs, and Kolar *et al.*,[8] whose focus is similar to ours (see below).

In the present paper we examine the implementation of normal flow (Neumann) conditions in the 3D context. We specifically focus on the 'Wave Equation' form of the 3D shallow water equations, as developed in 3D by Lynch and Werner[9,10] and Lynch *et al.*[2,11] for implementation on simple C^0 elements. Our objective is to achieve a workable approach with the following properties:

Correspondence to: D. R. Lynch, Dartmouth College, Hanover, NH, U.S.A.

Contract grant sponsor: USGLOBEC Program
Contact grant sponsor: Gulf of Maine Regional Marine Research Program
Contract grant sponsor: New Hampshire Sea Grant College Program

CCC 0271–2091/97/101185–21 $17.50

Received 29 May 1996
Revised 13 February 1997

(a) global mass conservation
(b) normal transport enforced strongly on the velocity solution at the boundary
(c) reversibility among Dirichlet (specified pressure) and Neumann (specified normal transport) problems.

Item (a) we take as a self-evident goal. Item (b) implies that boundary transports which appear in mass balance relationships will in fact be properties of the velocity solution. Item (c) addresses the equivalence between discrete solutions of the Dirichlet and Neumann problems and effectively demands that both problems be governed by an identical set of boundary constraints.

These issues were examined previously[12] in a simpler 2D, harmonic-in-time context. In that study, mass conservation was proven and a strong, reversible procedure demonstrated which eliminated $O(h)$ errors in conventional velocity solutions. Comparisons with an analytic solution confirmed that accuracy was upgraded from $O(h)$ to $O(h^2)$. Kolar *et al.*[8] generally confirmed these findings in a 2D time-stepping context, although the strong enforcement of Neumann conditions was not pursued. The result was a velocity discontinuity at the boundary, with the velocity solution retaining the $O(h)$ errors and only weakly connected to the mass-conserving boundary fluxes.

We find here that it is possible to meet all three goals for the general 3D time-stepping case; and that doing so provides superior solutions. We present a theoretical proof of the mass balance property, a discussion of implementation issues and idealized test cases which demonstrate the quality and reversibility of the solutions. We also include a practical example wherein an awkward boundary condition problem is addressed. Throughout we focus on a hydrostatic, Boussinesq fluid; thus wave propagation occurs in the horizontal only and volume and mass conservation are synonymous.

2. MASS BALANCE RELATIONS

2.1. Continuous-time domain

We first establish a basic conservation property of the weighted residual method used in conjunction with the wave equation. The basic idea is that of Lynch;[12] here we develop it further in the general context of 3D time domain solutions.

We begin with the continuity equation in 3D:

$$\nabla \cdot \mathbf{v} = \frac{\sigma}{\rho}, \tag{1}$$

and its vertical integral

$$\frac{\partial H}{\partial t} + \nabla_{xy} \cdot \int_{-h}^{\zeta} \mathbf{v}\, \mathrm{d}z = r, \tag{2}$$

where $\mathbf{v}(x, y, z, t)$ is the fluid velocity, $\zeta(x, y, t)$ is the free surface elevation, $h(x, y)$ is the bathymetric depth, $H(x, y, t)$ is the total fluid depth $H = h + \zeta$, σ/ρ is the volumetric source rate (fluid volume/time/unit volume) and r is the vertically integrated source term $\int_{-h}^{\zeta} (\sigma/\rho)\, \mathrm{d}z$ plus net precipitation at the free surface. The essence of the wave equation formulation is to use the time derivative of (2) to compute H:

$$\frac{\partial^2 H}{\partial t^2} + \tau_0 \frac{\partial H}{\partial t} + \nabla_{xy} \cdot \left[\left(\frac{\partial}{\partial t} + \tau_0 \right) \int_{-h}^{\zeta} \mathbf{v}\, \mathrm{d}z \right] = \left(\frac{\partial}{\partial t} + \tau_0 \right) r, \tag{3}$$

with τ_0 a numerical constant.* The weak form of (3) of interest here is the weighted residual with test function ϕ_i,

$$\left\langle \frac{\partial^2 H}{\partial t^2}\phi_i \right\rangle + \left\langle \tau_0 \frac{\partial H}{\partial t}\phi_i \right\rangle - \left\langle \nabla\phi_i \cdot \left[\left(\frac{\partial}{\partial t} + \tau_0 \right) \int_{-h}^{\zeta} \mathbf{v}\, \mathrm{d}z \right] \right\rangle + \oint \left(\frac{\partial}{\partial t} + \tau_0 \right) q\phi_i \, \mathrm{d}s = \left\langle \left(\frac{\partial}{\partial t} + \tau_0 \right) r\phi_i \right\rangle, \quad (4)$$

where $\langle , \rangle$ is the inner product notation (domain integration); $\oint \mathrm{d}s$ is the related line integral enclosing the domain; and q is the normal component of transport across the boundary, directed out of the domain. Here it is convenient to introduce the boundary transport integral Q_i and to re-express (4):

$$Q_i \equiv \oint q\phi_i \, \mathrm{d}s, \quad (5)$$

$$\left\langle \frac{\partial^2 H}{\partial t^2}\phi_i \right\rangle + \left\langle \tau_0 \frac{\partial H}{\partial t}\phi_i \right\rangle - \left\langle \nabla\phi_i \cdot \left[\left(\frac{\partial}{\partial t} + \tau_0 \right) \int_{-h}^{\zeta} \mathbf{v}\, \mathrm{d}z \right] \right\rangle + \left(\frac{\partial}{\partial t} + \tau_0 \right) Q_i = \left\langle \left(\frac{\partial}{\partial t} + \tau_0 \right) r\phi_i \right\rangle. \quad (6)$$

We require that the test functions be C^0 continuous on the domain and in addition have the property $\sum \phi_i = 1$, and therefore $\sum \nabla\phi_i = 0$, everywhere. Summing all the equations (6), we obtain the basic global mass balance

$$\left\langle \frac{\partial^2 H}{\partial t^2} \right\rangle + \left\langle \tau_0 \frac{\partial H}{\partial t} \right\rangle + \left(\frac{\partial}{\partial t} + \tau_0 \right) \oint q \, \mathrm{d}s = \left\langle \left(\frac{\partial}{\partial t} + \tau_0 \right) r \right\rangle. \quad (7)$$

We introduce the following simple notation: $S = \langle H \rangle$ is the total mass in the system, $Q = \sum Q_i = \oint q \, \mathrm{d}s$ is the rate of mass efflux from the system, $R = \langle r \rangle$ is the rate of mass creation within the system and $I = \mathrm{d}S/\mathrm{d}t + Q - R$ is the system-wide mass imbalance. In these terms, (7) becomes

$$\frac{\mathrm{d}I}{\mathrm{d}t} + \tau_0 I = 0, \quad (8)$$

$$I = I_0 \mathrm{e}^{-\tau_0 t}. \quad (9)$$

Clearly, the analytic solution has $I = 0$ always and the weak form (6) will have this property provided that I is initially zero, i.e. the initial conditions are in balance. If not, then the imbalance will be eliminated at the rate τ_0. Round-off error accumulated in the mass balance will be removed at the same rate.

This mass balance is valid for any quadrature approximation to the integrals $\langle \ \rangle$ and $\oint \mathrm{d}s$ provided that all terms of the weighted residual are evaluated with the same quadrature in any given element. The specific quadrature used defines the integrations of the global quantities S, Q, R and I.

Implementation of these ideas in 2D, harmonic-in-time circulation models is described in Reference 12 and corroborated in other applications (e.g. References 13 and 14).

1. *Neumann conditions.* Here q is know *a priori*. The Neumann data are inserted directly into the boundary integral in (6), supporting the solution for H. The same data are used as a strong constraint on the velocity, i.e. $\int_{-h}^{\zeta} \mathbf{v} \cdot \hat{\mathbf{n}} \, \mathrm{d}z$ is specified.
2. *Dirichlet conditions.* Here q is unknown *a priori*, but H is known. The reduced system of weighted residuals is solved for H in the conventional way; then the 'neglected' WR equations are used to compute the boundary integrals $(\partial/\partial t + \tau_0)Q_i$, which is then used to constrain the velocity exactly as in the Neumann problem.

* The momentum equation is eventually substituted for the divergence term in (3), but that will not matter here.

In this way we achieve perfect reversibility between Neumann and Dirichlet problems, since the same relations are used in both cases, and retain in either case the global mass balance*.

The relations among the boundary quantities (Q, q) and the domain solution $\mathbf{v}$ need to be clearly defined if the mass balance (8) is to be useful. With $\mathbf{v}$ expanded in the horizontal basis ϕ, $\mathbf{v}(x, y, z, t) = \sum \mathbf{v}_j(z, t)\phi_j(x, y)$, we have

$$Q_i = \sum \int_{-h}^{\zeta} \mathbf{v}_j \, \mathrm{d}z \cdot \oint \hat{\mathbf{n}}\phi_j\phi_i \, \mathrm{d}s \tag{10}$$

or equivalently, with $\mathbf{N}_{ij} = \oint \hat{\mathbf{n}}\phi_i\phi_j \, \mathrm{d}s$,

$$Q_i = \sum \int_{-h}^{\zeta} \mathbf{v}_j \, \mathrm{d}z \cdot \mathbf{N}_{ij}. \tag{11}$$

Throughout the preceding 3D model development[2,9,10] we have routinely used quadrature points located at the nodes of simple linear elements, which has the effect of lumping mass matrices such as the one defining $\mathbf{N}_{ij}$ here. With nodal quadrature, equation (10) reduces to the simple form

$$Q_i = \mathbf{N}_i \cdot \int_{-h}^{\zeta} \mathbf{v}_i \, \mathrm{d}z = \Delta s_i \hat{\mathbf{n}}_i \cdot \int_{-h}^{\zeta} \mathbf{v}_i \, \mathrm{d}z, \tag{12}$$

with $\mathbf{N}_i = [\Delta s_1 \hat{\mathbf{n}}_1 + \Delta s_2 \hat{\mathbf{n}}_2]$ the quadrature approximation to $\mathbf{N}_{ii}$. Its unit vector $\hat{\mathbf{n}}_i$ is the 'nodal normal'; its magnitude Δs_i is an effective local boundary segment. These quantities are illustrated in Figure 1(a) for simple linear elements. The nodal normal so defined has been widely used since the early FEM investigations.[15,16]

It is important to note that for a straight boundary, $\hat{\mathbf{n}}_i$ is unambiguous and Δs_i is simply one-half of the sum of adjacent boundary element lengths. Discretized boundary curvature effectively shortens Δs_i as in Figure 1(a), and the nodal normal favours the longer adjacent boundary element.

The constraint on velocity is simply equation (12) in reverse:

$$\hat{\mathbf{n}}_i \cdot \int_{-h}^{\zeta} \mathbf{v}_i \, \mathrm{d}z = \frac{Q_i}{\Delta s_i} = q_i, \tag{13}$$

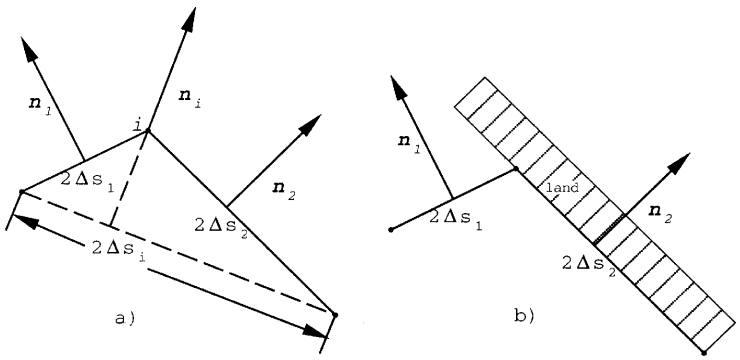

Figure 1. Nodal normal $\hat{\mathbf{n}}_i$ and boundary segment Δs_i: (a) common boundary with curvature; (b) corner

* The 'conventional' implementation of Dirichlet boundary conditions (H known), wherein the local weighted residual equations are not enforced, loses the property $\sum \phi_i = 1$ and therefore the mass balance is compromised.

whereby q_i, the nodal transport, is defined. At a corner, as illustrated in Figure 1(b), we have the additional constraint

$$\hat{\mathbf{n}}_2 \cdot \int_{-h}^{\zeta} \mathbf{v}_i \, \mathrm{d}z = 0. \tag{14}$$

This is enforced simultaneously with equation (13). Together they imply the equivalent pair of constraints

$$\hat{\mathbf{n}}_1 \cdot \int_{-h}^{\zeta} \mathbf{v}_i \, \mathrm{d}z = \frac{Q_i}{\Delta s_1}, \tag{15}$$

$$\hat{\mathbf{n}}_2 \cdot \int_{-h}^{\zeta} \mathbf{v}_i \, \mathrm{d}z = 0, \tag{16}$$

which is perhaps more appealing intuitively.

This general procedure is directly applicable to the 3D time domain case. What remain to be shown are (a) a temporal discretization for the boundary transports and the resulting discrete-time mass balance and (b) a method for constraining the 3D velocity field $\mathbf{v}_i(z)$ with the 2D Neumann data q_i.

2.2. *Time domain discretization*

The discrete-time form of (6) is obtained by conventional second-order finite difference approximations. Introducing time levels $k-1$, k, and $k+1$ separated by uniform Δt, we have

$$\frac{\partial H}{\partial t} = \frac{H^{k+1} - H^{k-1}}{2\Delta t}, \tag{17}$$

$$\frac{\partial^2 H}{\partial t^2} = \frac{H^{k+1} - 2H^k + H^{k-1}}{\Delta t^2} \tag{18}$$

or equivalently, using $\Delta H^k \equiv H^k - H^{k-1}$ (the change in storage over time step k),

$$\frac{\partial H}{\partial t} = \frac{\Delta H^{k+1} + \Delta H^k}{2\Delta t}, \tag{19}$$

$$\frac{\partial^2 H}{\partial t^2} = \frac{\Delta H^{k+1} - \Delta H^k}{\Delta t^2}. \tag{20}$$

Additionally, we introduce the boundary transport $\bar{Q}_i^k$ as a discrete representation of the total normal transport over the time step k, i.e.

$$\Delta t \bar{Q}_i^k = \int_{k-1}^{k} Q_i \, \mathrm{d}t = \Delta t[\varepsilon Q_i^k + (1-\varepsilon) Q_i^{k-1}], \tag{21}$$

and similarly for $\bar{r}^k$. An appropriate discretization of the boundary flux in equation (6), centred at time k, is

$$\left(\frac{\partial}{\partial t} + \tau_0\right) Q_i = \frac{\bar{Q}_i^{k+1} - \bar{Q}_i^k}{\Delta t} + \tau_0 \frac{\bar{Q}_i^{k+1} + \bar{Q}_i^k}{2}. \tag{22}$$

(It is assumed that $\bar{Q}_i^0$ is known or computable from the initial conditions. Recall that wave equation algorithms require initial conditions at two time levels.)

Substitution of these difference expressions into (6) gives the complete discrete-time form of equation (6):

$$\left\langle \frac{1}{\Delta t}\left(\frac{\Delta H^{k+1}}{\Delta t}-\frac{\Delta H^{k}}{\Delta t}\right)\phi_i\right\rangle+\left\langle \tau_0\left(\frac{\Delta H^{k+1}}{2\Delta t}+\frac{\Delta H^{k}}{2\Delta t}\right)\phi_i\right\rangle-\left\langle \nabla\phi_i\cdot\left[\left(\frac{\partial}{\partial t}+\tau_0\right)^k\int_{-h}^{\zeta}\mathbf{v}\,\mathrm{d}z\right]\right\rangle$$
$$=-\left(\frac{\bar{Q}_i^{k+1}-\bar{Q}_i^{k}}{\Delta t}+\tau_0\frac{\bar{Q}_i^{k+1}+\bar{Q}_i^{k}}{2}\right)+\left\langle\left(\frac{\bar{r}^{k+1}-\bar{r}^{k}}{\Delta t}+\tau_0\frac{\bar{r}^{k+1}+\bar{r}^{k}}{2}\right)\phi_i\right\rangle. \tag{23}$$

Summing as above, we obtain the discrete-time mass balance

$$\frac{1}{\Delta t}\left(\frac{\Delta S^{k+1}}{\Delta t}-\frac{\Delta S^{k}}{\Delta t}\right)+\tau_0\left(\frac{\Delta S^{k+1}}{2\Delta t}+\frac{\Delta S^{k}}{2\Delta t}\right)+\frac{\bar{Q}^{k+1}-\bar{Q}^{k}}{\Delta t}+\tau_0\frac{\bar{Q}^{k+1}+\bar{Q}^{k}}{2}=\frac{\bar{R}^{k+1}-\bar{R}^{k}}{\Delta t}+\tau_0\frac{\bar{R}^{k+1}+\bar{R}^{k}}{2} \tag{24}$$

where, as above, $\Delta t\bar{Q}^k$ is the total transport into the system during time step k, i.e.

$$\Delta t\bar{Q}^k\equiv\int_{k-1}^{k}Q\,\mathrm{d}t, \tag{25}$$

and similarly for $\bar{R}^k$. We introduce the discrete system mass imbalance, integrated over time step k,

$$I^k\equiv\Delta S^k+\Delta t\bar{Q}^k-\Delta t\bar{R}^k, \tag{26}$$

and (24) reduces to

$$I^{k+1}-I^k+\frac{\tau_0\Delta t}{2}(I^{k+1}+I^k)=0, \tag{27}$$

$$I^{k+1}=I^k\left(\frac{1-\tau_0\Delta t/2}{1+\tau_0\Delta t/2}\right). \tag{28}$$

Equation (28) is clearly a discrete-time form of (9), to which it converges in the limit of infinitesimal Δt.* It has the analogous properties: mass imbalance introduced through either initial conditions or round-off will decay unconditionally. In addition, we observe that the decay will be monotone for $\tau_0\Delta t<2$ and oscillatory (but stable) for larger time steps.

3. IMPLEMENTATION IN 3D

We introduce here the 3D momentum equation

$$\frac{\partial\mathbf{v}}{\partial t}+\mathbf{f}\times\mathbf{v}-\frac{\partial}{\partial z}\left(N\frac{\partial\mathbf{v}}{\partial z}\right)=-\frac{1}{\rho}\nabla P+\mathbf{F} \tag{29}$$

* Note that $\left(\frac{1-\tau_0\Delta t/2}{1+\tau_0\Delta t/2}\right)=\mathrm{e}^{-\tau_0\Delta t}+O(\tau_0\Delta t)^3$.

and its vertical boundary conditions

$$N\frac{\partial \mathbf{v}}{\partial z}\bigg|_{z=\zeta} = H\boldsymbol{\Psi}, \tag{30}$$

$$\left(N\frac{\partial \mathbf{v}}{\partial z} - K\mathbf{v}\right)\bigg|_{z=-h} = 0, \tag{31}$$

where f is the Coriolis parameter, N is the eddy viscosity, and P is the pressure. Advective nonlinearities and horizontal viscous terms are assumed to be treated explicitly in a time step, included in $\mathbf{F}$. $H\boldsymbol{\Psi}$ is the known atmospheric stress and K is a bottom slip coefficient linearized over the time step. This system is solved as a 1D ODE for the function $\mathbf{v}_i(z)$ at each horizontal node i.

The specific time discretization we employ has the linear terms centred in the time step and $\mathbf{R}$ explicit. The average velocity over a time step, $\bar{\mathbf{v}}_i^{k+1}$, is defined for convenience as

$$\bar{\mathbf{v}}_i^{k+1} = \frac{\mathbf{v}_i^{k+1} + \mathbf{v}_i^k}{2}, \tag{32}$$

$$\Delta\mathbf{v}_i^{k+1} \equiv \mathbf{v}_i^{k+1} - \mathbf{v}_i^k = 2\bar{\mathbf{v}}_i^{k+1} - 2\mathbf{v}_i^k. \tag{33}$$

The discrete form of (29)–(31) is then

$$\left[\frac{2}{\Delta t} + \mathbf{f}\times - \frac{\partial}{\partial z}\left(N\frac{\partial}{\partial z}\right)\right]\bar{\mathbf{v}}_i^{k+1} = \left(\frac{2\mathbf{v}_i}{\Delta t} + \mathbf{F}_i\right)^k - \frac{1}{\rho}\nabla P_i, \tag{34}$$

$$N\frac{\partial \bar{\mathbf{v}}_i^{k+1}}{\partial z}\bigg|_{z=\zeta} = H\boldsymbol{\Psi}_i, \tag{35}$$

$$\left(N\frac{\partial}{\partial z} - K\right)\bar{\mathbf{v}}_i^{k+1}\bigg|_{z=-h} = 0. \tag{36}$$

3.1. The Neumann problem

For the 2D equations the Neumann problem is trivial. The given Neumann data q are entered in the boundary integral in (6) for H. The tangential portion of the momentum equation is enforced, with the constraint $H\mathbf{v}\cdot\hat{\mathbf{n}} = q$. The normal momentum equation is sacrificed in the process. Note that the tangential velocity is also affected, since it is coupled to the normal velocity through the Coriolis term.

In 3D we have the problem of enforcing q on the vertical integral of $\mathbf{v}$. Because of the Coriolis term, both normal and tangential force balances couple throughout the water column and a more subtle approach is needed. We approach this problem by observing that *the normal component of the pressure gradient in* (29) *is imperfect*, consisting of one-sided derivatives and lacking any direct boundary condition information. *We therefore correct the pressure gradient with an additional normal-directed barotropic component, sufficient to produce the known normal transport*:

$$\frac{1}{\rho}\nabla P = \frac{1}{\rho}\nabla P_{\mathrm{I}} + \alpha\hat{\mathbf{n}}, \tag{37}$$

where ∇P_{I} is the 'interior', imperfect pressure gradient and α is to be determined. To do this, we solve (34)–(36) twice: once as written, with $\alpha = 0$, for the conventional or 'interior' velocity; and a second 'exterior' solution driven only by a unit barotropic pressure gradient normal to the boundary, with

homogeneous boundary conditions. The two solutions are then superposed with enforcement of the normal transport dictating the parameter α.

Equation (34) is solved for the internal solution $\bar{\mathbf{v}}_{\mathrm{I}}^{k+1}$:

$$\left[\frac{2}{\Delta t}+\mathbf{f}\times-\frac{\partial}{\partial z}\left(N\frac{\partial}{\partial z}\right)\right]\bar{\mathbf{v}}_{\mathrm{I}i}^{k+1}=\left(\frac{2\mathbf{v}}{\Delta t}+\mathbf{F}\right)_i^k-\frac{1}{\rho}\nabla P_{\mathrm{I}i}, \tag{38}$$

subject to the boundary conditions (35) and (36). This is exactly the conventional velocity calculation. The same linear operator applies to the external solution $\bar{\mathbf{v}}_{\mathrm{E}}^{k+1}$:

$$\left[\frac{2}{\Delta t}+\mathbf{f}\times-\frac{\partial}{\partial z}\left(N\frac{\partial}{\partial z}\right)\right]\bar{\mathbf{v}}_{\mathrm{E}i}^{k+1}=-\hat{\mathbf{n}}_i, \tag{39}$$

subject to homogeneous boundary conditions (i.e. equation (35) with $H\boldsymbol{\Psi}=0$ and equation (36) which is already homogeneous). The complete solution is then

$$\bar{\mathbf{v}}_i^{k+1}=[\bar{\mathbf{v}}_{\mathrm{I}}^{k+1}+\alpha\bar{\mathbf{v}}_{\mathrm{E}}^{k+1}]_i, \tag{40}$$

with α given by the requirement that $\hat{\mathbf{n}}\cdot\int_{-h}^{\zeta^{k+1}}\mathbf{v}^{k+1}\,\mathrm{d}z=q^{k+1}$:

$$\alpha_i=\left[\frac{q^{k+1}-\hat{\mathbf{n}}\cdot\int_{-h}^{\zeta^{k+1}}(2\bar{\mathbf{v}}_{\mathrm{I}}^{k+1}-\mathbf{v}^k)\,\mathrm{d}z}{\hat{\mathrm{n}}\cdot\int_{-h}^{\zeta^{k+1}}2\bar{\mathbf{v}}_{\mathrm{E}}^{k+1}\,\mathrm{d}z}\right]_i. \tag{41}$$

Two sequential solutions are thus required, using the same linear operator. Their superposition according to (32), (40) and (41) completes the time step in the conventional way:

$$\mathbf{v}_i^{k+1}=2\bar{\mathbf{v}}_i^{k+1}-\mathbf{v}_i^k. \tag{42}$$

3.2. *The Dirichlet problem*

In this problem, q is not known *a priori*, rather H is known. Our approach is to deduce the equivalent Neumann data and to enforce them on the velocity solution as described above. We solve the system of wave equations (23) with the Dirichlet data enforced and the corresponding WR equations removed. The boundary integrals

$$B_i\equiv\Delta s_i\left(\frac{\overline{q}_i^{k+1}-\overline{q}_i^k}{\Delta t}+\tau_0\frac{\bar{q}_i^{k+1}+\bar{q}_i^k}{2}\right)$$

are then evaluated with the unused WR equations (23), enabling extraction of $\bar{q}_i^{k+1}$. We then obtain the transport at the end of the time step:

$$q_i^{k+1}=\frac{\overline{q}_i^{k+1}-(1-\varepsilon)q_i^k}{\varepsilon}. \tag{43}$$

The velocity calculation may proceed exactly as in the Neumann case. Effectively, we have identified the equivalent Neumann data for the Dirichlet problem.

Note that equation (43) contains a homogeneous mode for the series q_i^{k+1} which will be unstable for $\varepsilon\leqslant\frac{1}{2}$. We confirm this in practice. In the problems below we used $\varepsilon=0.53$, which we have found to be generally suitable.

4. TEST PROBLEM 1

The first case is intended to demonstrate (a) the significant impact of the mass-conserving BC on the velocity solution, relative to conventional practice, and (b) the reversibility of the Dirichlet and Neumann problems. To do this, we use a simple rectangular domain (Figure 2). Typical of many practical studies, there are extensive open-water boundaries and apparently simple boundary conditions on pressure that support complex patterns of subtidal flow through an essentially open system. We use large-amplitude tidal forcing here to enhance the subtidal motions through non-linear tidal rectification.

The general parameters for this problem are as follows.

1. Depth decreases linearly from the coast to the offshore boundary, from 10 to 55 m.
2. Latitude is 43·5°.
3. Land boundary conditions are no normal flow throughout the vertical.
4. There is no wind forcing and the mass fields are homogeneous.

Dirichlet boundary conditions were imposed in terms of periodic (M2) plus residual elevation as in Figure 7. The results are shown in Figures 3–5, after periodicity had been achieved. In Figure 3, a time series of one period in length is shown of the vertically averaged velocity and $g\nabla\zeta_I \cdot \hat{\mathbf{n}}$ at nodes 1 and 9 (see Figure 2 for location) for the simulation with the conventional formulation. In Figure 4 a similar set of time series is shown for the mass-conserving simulation. Note in Figure 4 that α (equation (37)) is also shown. In the node 1 and 9 plots a significant increase can be seen in the y-direction velocity of the mass-conserving simulation. The x-direction velocity of node 1 is zero because of the land boundary. The difference in node 9 of the x-direction velocity is caused by the coupling of the x- and y-direction velocities through the Coriolis force. The plots of $g\nabla\zeta_I \cdot \hat{\mathbf{n}}$ and α show clearly that the conventional formulation has not captured the correct pressure gradient at the boundary. In Figure 5, plots of the residual vertically averaged velocity for the two formulations are shown. As expected the internal solution is not greatly changed, but closer to the boundary some

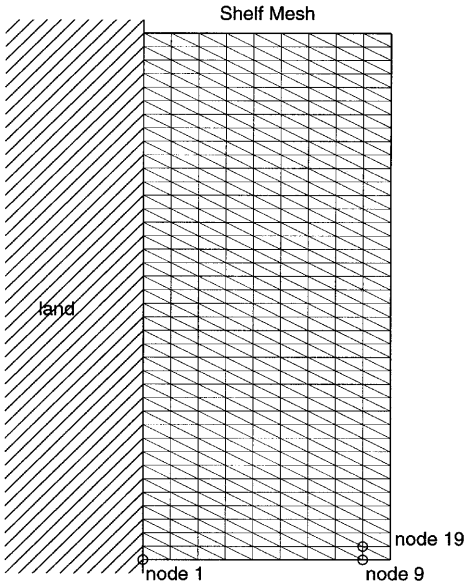

Figure 2. Shelf mesh—width 18 km, length 39 km, $\Delta x = 2$ km, $\Delta y = 1$ km

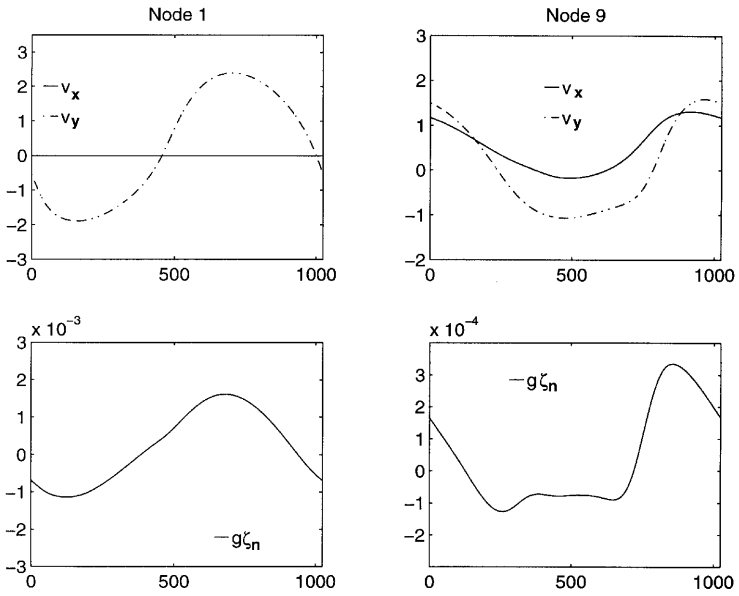

Figure 3. Conventional formulation time series of one period: left panels, node 1; right panels, node 9; top panels, vertically averaged velocity; bottom panels, $g\nabla\zeta_I \cdot \hat{\mathbf{n}}$

significant differences can be found. The mass-conserving formulation has at node 19 (see Figure 2 for location) an increase of 0·3072 m s^{-1} in the residual vertically averaged speed (refer to Figure 5). In the M2 constituent the maximum increase was at node 1 with a value of 0·9190 m sec^{-1} (refer to Figures 3 and 4).

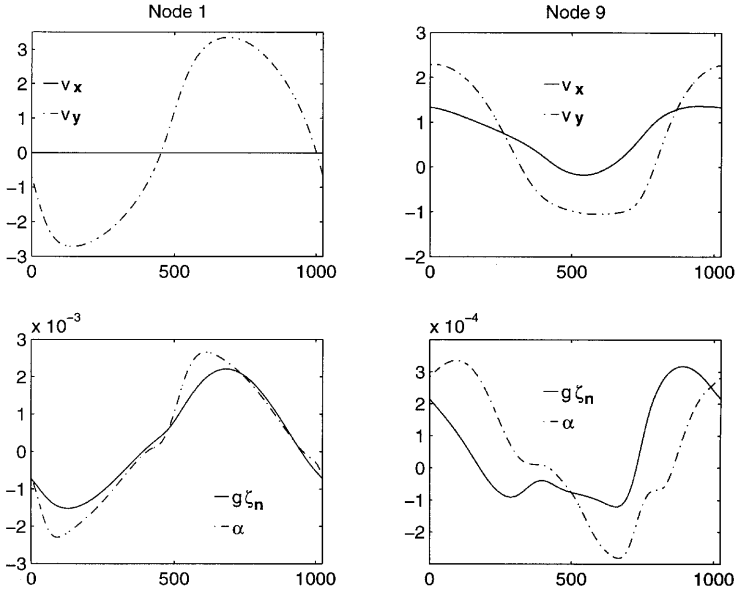

Figure 4. Mass-conserving formulation time series: convention same as Figure 3, but bottom panels also include α

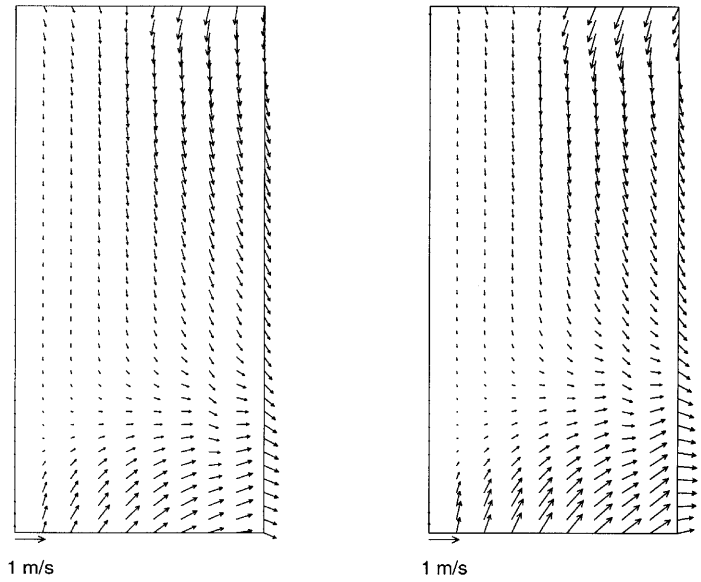

Figure 5. Residual vertically averaged velocity with Dirichlet boundary conditions: left panel, conventional formulation; right panel, mass-conserving formulation

Neumann BCs were obtained as a periodic time series of q from the above solution. Interestingly, these time series contained higher harmonics of the M2 constituent, as expected for a non-linear simulation (see e.g. Figure 4). The time series q was used to force a second solution, initialized from the Dirichlet solution in periodic steady state. Results appear in Figures 6 and 7. The reversibility of

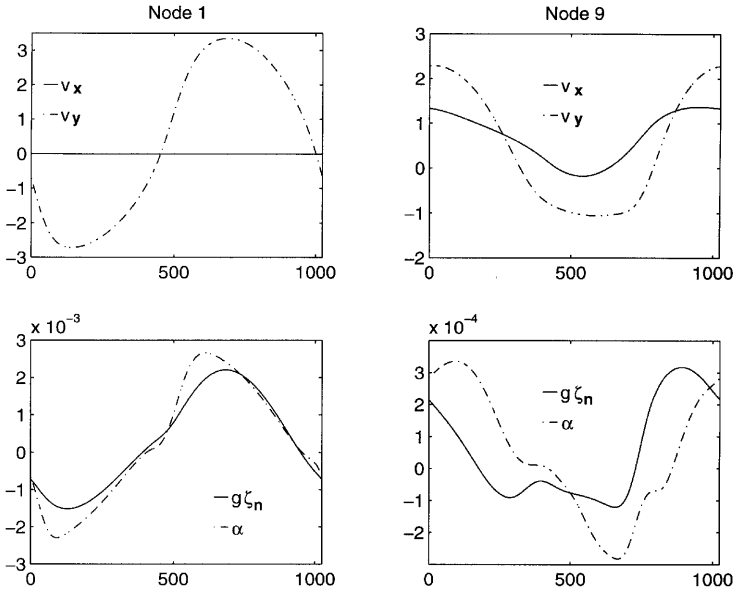

Figure 6. Mass-conserving formulations with Neumann boundary condition time series: convention same as Figure 4

the two approaches is demonstrated by the retrieval of the original Dirichlet solution on the boundary. Figure 7 shows the recovery of the M2 and residual constituents; higher harmonics were negligible. Further confirmation of the reversibility is the reproduction of the velocity and pressure gradient time series—compare Figures 6 and 4.

Global mass balance for this simulation is demonstrated in Figure 8. Therein we display time series for the two quantities

$$\int\int \zeta \, \mathrm{d}x \, \mathrm{d}y \quad \text{and} \quad \int_0^t \oint \int_{-h}^{\zeta} \mathbf{v} \cdot \hat{\mathbf{n}} \, \mathrm{d}z \, \mathrm{d}s \, \mathrm{d}t'$$

and their difference, beginning from initial conditions (at rest) and continuing through one tidal period. The mass balance is confirmed even in the presence of start-up 'wiggles'.

In addition to its global property, the mass-conserving boundary condition generally provides improved local solutions. To illustrate this, we have severed the mesh of Test problem 1 as shown in

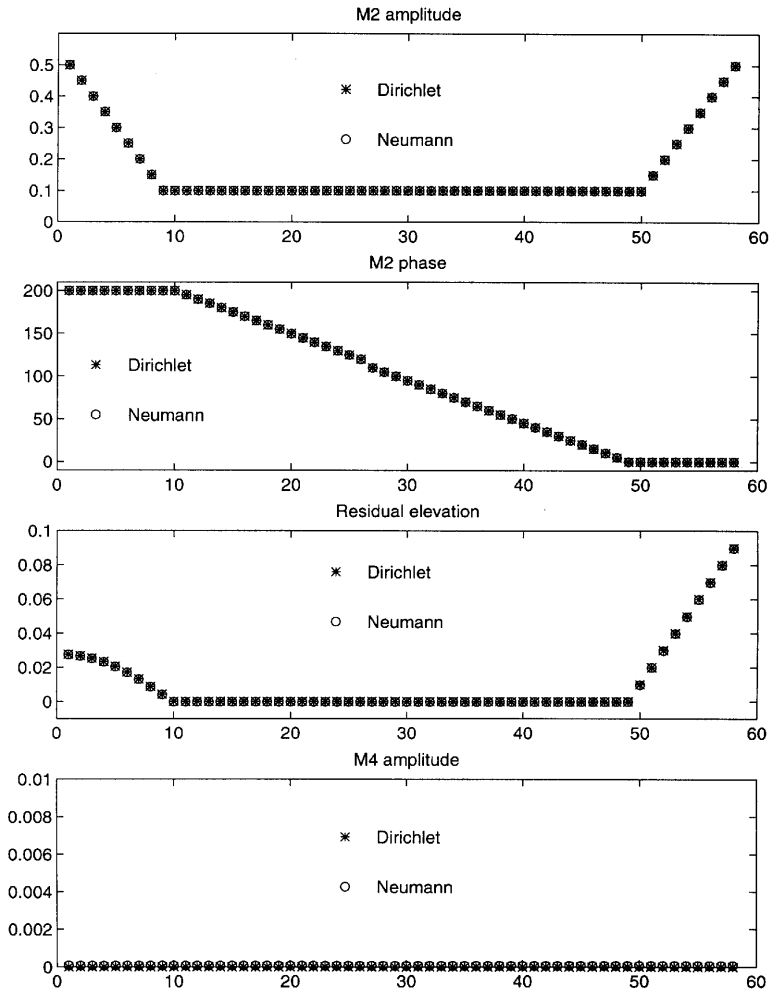

Figure 7. Elevation boundary conditions used to force Dirichlet simulation, and boundary elevations obtained from Neumann simulation. The two simulations are identical even in the physically unrealistic corner areas (e.g. nodes 9 and 10)

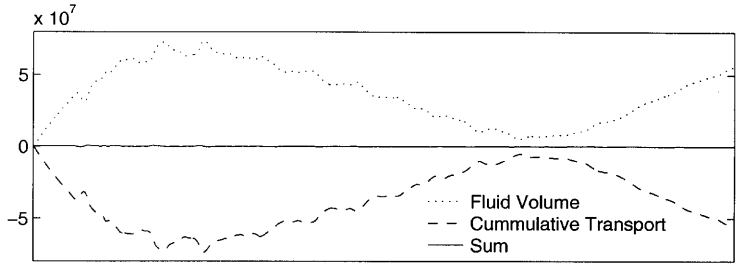

Figure 8. Comparison of $\int\int \zeta \, dx \, dy$ and $\int_0^t \oint \int_{-h}^{\zeta} \mathbf{v} \cdot \hat{\mathbf{n}} \, dz \, ds \, dt'$ for Test problem 1. The system is started from rest at $t = 0$. The first tidal period (1024 time steps) is plotted

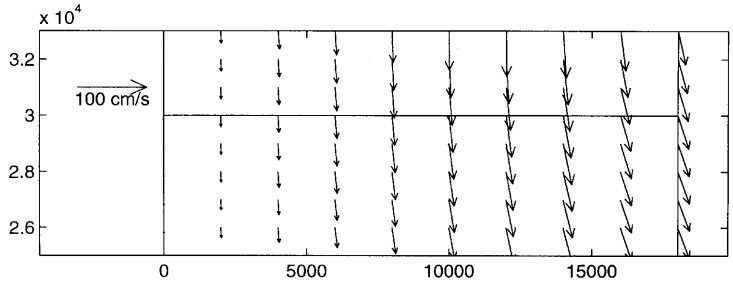

Figure 9. Illustration of cut in mesh of Test problem 1, along with tidally and vertically averaged velocities. This is the prototype for evaluating the calculations shown in Figures 10 and 11

Figure 9 and simulated the same problem on the lower portion. Initial conditions were taken from the large-mesh simulation once periodic steady state was reached; Dirichlet boundary conditions across the top boundary were taken from the same solution. The resulting velocities are shown in Figures 10 and 11 for conventional and mass-conserving velocity calculations along the top boundary. The mass-conserving calculation is clearly faithful to the prototype, with the flow entering smoothly along the top boundary. The conventional boundary velocity calculations show a systematic veering relative to the prototype. (In both cases, mass-conserving Dirichlet conditions are enforced on the other two open boundaries.)

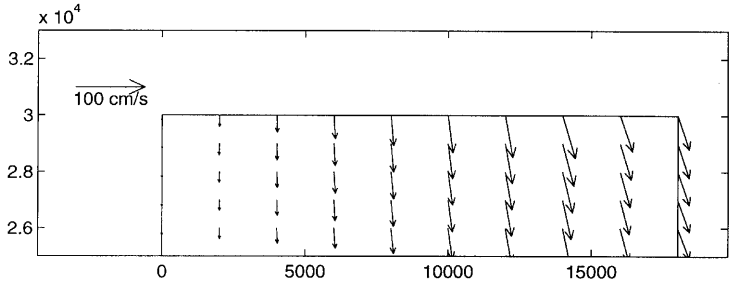

Figure 10. Velocity obtained on truncated Test problem 1 mesh with mass-conserving Dirichlet conditions across top boundary. The velocity is generally in agreement with the prototype, Figure 9

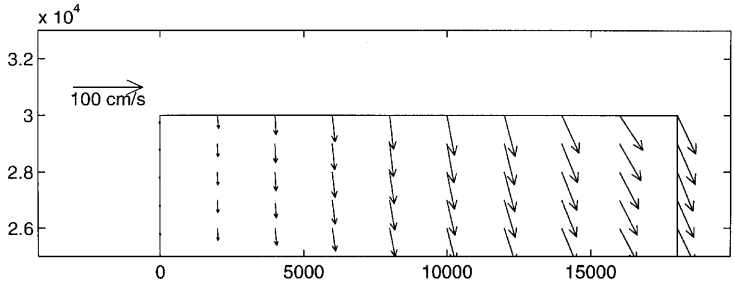

Figure 11. Same as Figure 10, except conventional Dirichlet conditions are enforced across top boundary. The velocity solution veers at the top boundary in comparison with Figure 9

5. TEST PROBLEM 2

The second case is inspired by a practical modelling problem we face in our Gulf of Maine studies[2] (see Figure 12). In this case there is a significant computational cost associated with computing the detailed local tidal resonance in the Bay of Fundy. The practical solution is to place an artificial boundary across the Bay of Fundy and drive the system with observed tidal elevation. This is entirely satisfactory for tides alone, but the subtidal motions associated with, for example, wind events would be artificially constrained by the Dirichlet BCs on pressure.

From a physical perspective the boundary is effectively impermeable at subtidal time scales. For example, in the following section we study a strong wind event lasting 60 h with elevation change of order 20 cm in the bay. The neglected area shown in the mesh of Figure 21 is roughly 4×10^9 m^2. Total transport across the bay boundary would therefore be approximately $0{\cdot}003 \times 10^6$ m^3 s^{-1} during such an event. This is negligible in the context of the seasonal mean circulation, wherein flows of order $0{\cdot}2 \times 10^6$ m^3 s^{-1} are circulating around the deeper portions of the bay included in the model.[17] The desired BC would therefore be a mixed one: Dirichlet BCs for tidal response and homogeneous Neumann BCs for the subtidal motions. Thus the unmodelled portion of the bay would resonate properly with the tide and would present a no-flow boundary to the subtidal motions, with subtidal pressure free to respond.*

In earlier studies using a harmonic-in-time model,[18,19] separate calculations are made at tidal and subtidal frequencies and therefore the mixed BC strategy is possible. In the time domain this option is not available. Instead, we exploit the reversibility of the Neumann and Dirichlet BCs developed here. The system is forced with periodic Neumann BCs (i.e. time-averaged normal transport equals zero), with the Neumann data obtained from (and equivalent to) a Dirichlet simulation with tides alone.

To illustrate this, we use the idealized mesh shown in Figure 13. The tidal boundary conditions are first approximated by a pure M2 Dirichlet condition across the bay boundary; typically this would be obtained from field observations. The Dirichlet simulation was run until periodic steady state was reached. The non-linearities created both higher harmonics and a small non-zero residual in the q-signals. These were filtered to retain only the M2, M4 and M6 constituents for q. The Neumann solution forced with these signals therefore did not match the original 'correct' Dirichlet solution perfectly, so the process was reiterated with a fuller elevation spectrum—including a non-zero residual elevation—for the Dirichlet problem. After two iterations a reasonable match was obtained—Figures 14 and 15—and the periodic q-signal with zero mean as illustrated in Figure 15 was adopted as the tidal forcing. The resulting residual transport patterns are illustrated in Figure 16.

* Note that a conventional radiation condition here, whereby an infinite ocean is presumed outside of the domain, would be inappropriate.

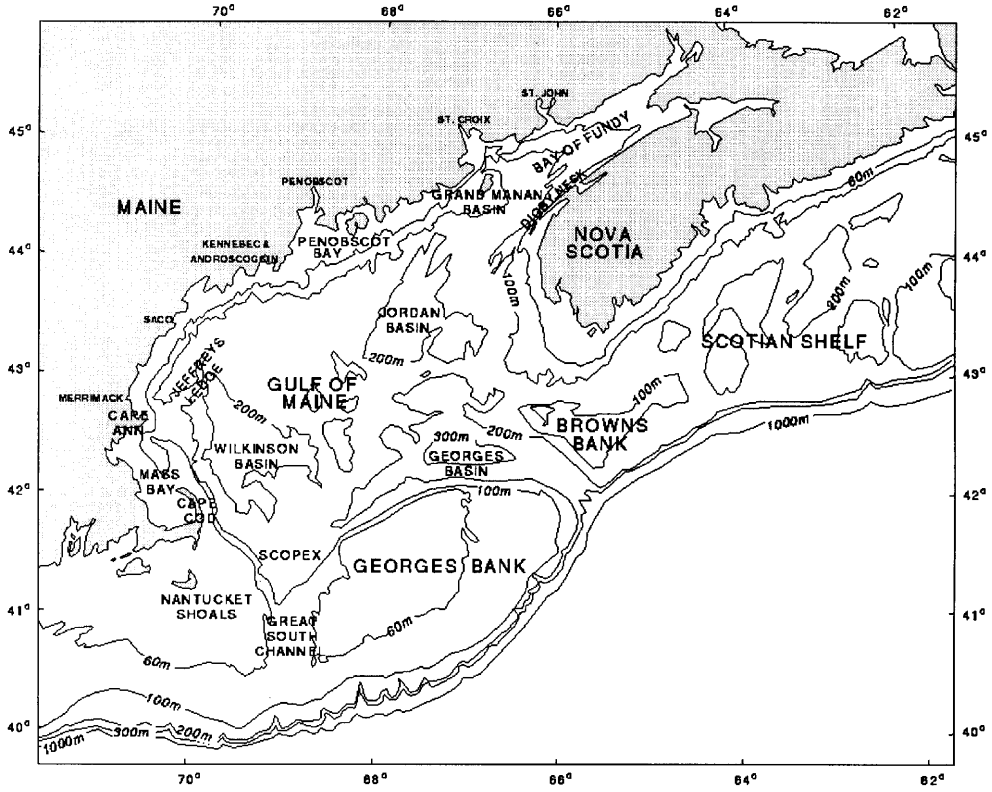

Figure 12. Gulf of Maine map

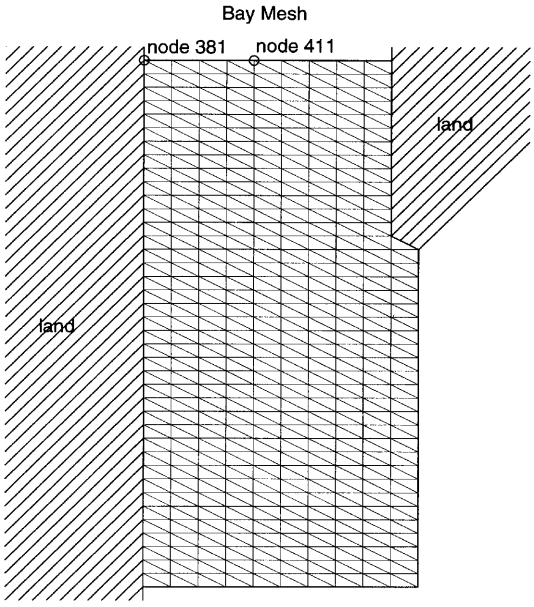

Figure 13. Bay mesh—width 20 km (at bottom) and 18 km (at top), length 39 km, $\Delta x = 2$ km, $\Delta y = 1$ km

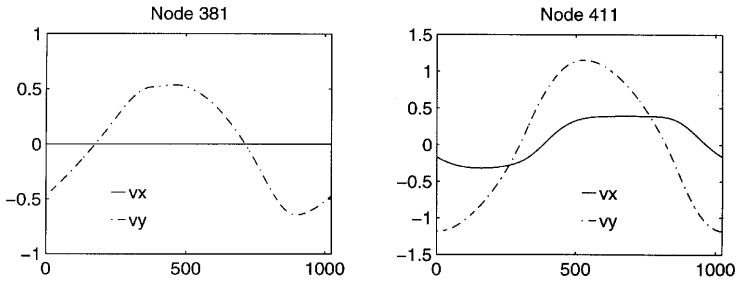

Figure 14. Dirichlet solution with residual elevation: vertically averaged velocity at nodes 381 and 411 (see Figure 13 for location)

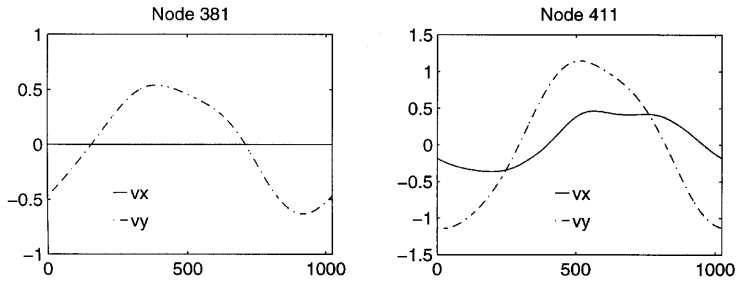

Figure 15. Neumann solution with M6, M4 and M2 transport: vertically averged velocity at nodes 381 and 411 (see Figure 13 for location)

This tidal forcing was used to simulate the effect of a steady wind plus tides on this mesh. Dirichlet conditions were used on the rest of the wet boundaries.* Results for the residual elevation appear in Figure 18 and may be contrasted with those in Figure 17 which was computed with Dirichlet conditions, i.e. with the residual pressure response clamped. The significant discrepancy between the two responses illustrates the importance of the Neumann condition in this context, wherein it is justified on physical grounds. In Figures 19 and 20 we show the residual transport along the bay boundary for the Dirichlet and Neumann conditions respectively.

6. FIELD-SCALE SIMULATION

This idea has been implemented on a realistic Gulf of Maine mesh (Figure 21) for a transient wind event. The wind forcing is taken from observed data for March 1986. (See Reference 20 for more information.) The mass fields are a climatological representation of the March–April season and the offshore boundary conditions are also seasonal. The Bay of Fundy cut is forced with the Dirichlet condition and compared with the physically correct Neumann condition (obtained as described in Test problem 2).

The main purpose of this case is to show aptitude in a realistic simulation under severe wind forcing. The most illustrative quantities to compare are the moving average normal residual transport and elevation at a node along the Bay of Fundy boundary (see Figure 21 for location). In Figure 22 these quantities are shown for both the Neumann and Dirichlet conditions, as well as the normal wind

* Residual elevation was zero on the eastern boundary and in approximate geostrophic balance on the southern boundary.

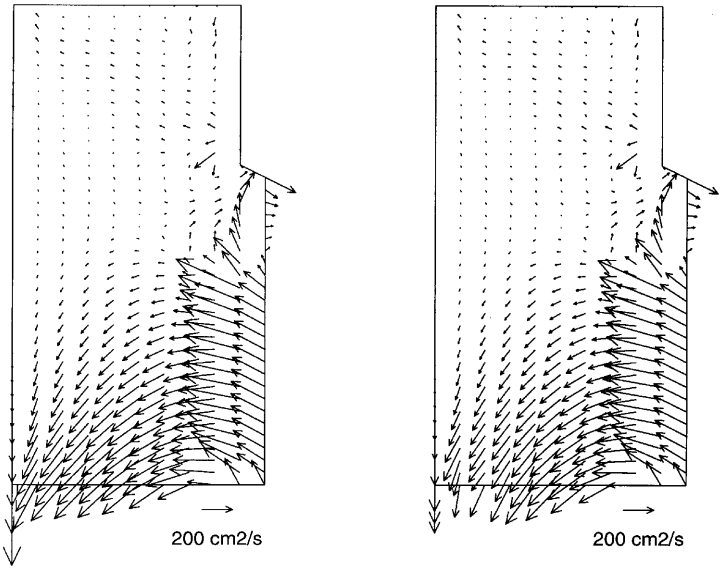

Figure 16. Residual transport forced by tide only. Left panel, Dirichlet condition; right panel, Neumann condition. Note the replication of even the short-wavelength 'noise' in the upper right corner

stress at the node. The moving average is done to eliminate the tidal response and therefore the results in Figure 22 show no net residual transport in the Neumann case and show constant elevation in the Dirichlet case.

The effect of the boundary condition can be seen in Figures 23 and 24 for Dirichlet and Neumann conditions respectively. In the Dirichlet case the 3D field is effectively flowing into an infinitely deep

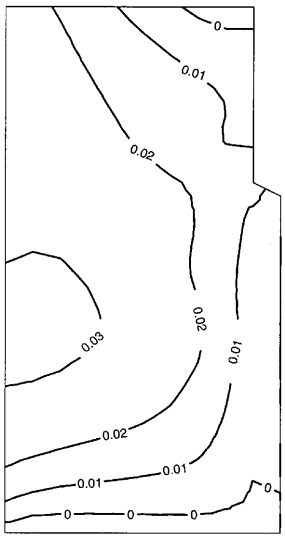

Figure 17. Residual elevation response with Dirichlet condition forced by tides and wind

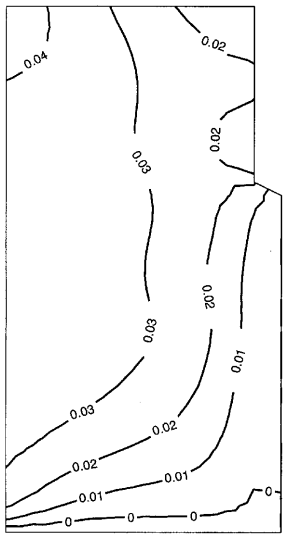

Figure 18. Residual elevation response with Neumann condition on bay forced by tides and wind

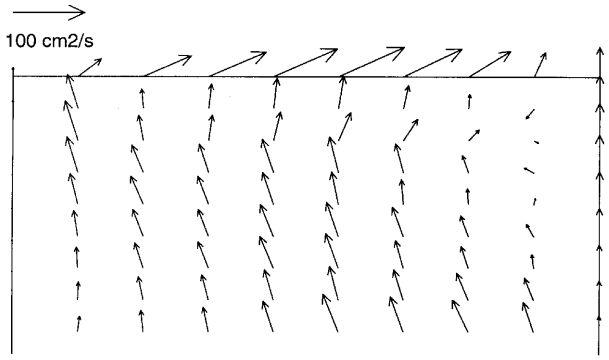

Figure 19. Residual transport of upstream region with Dirichlet condition

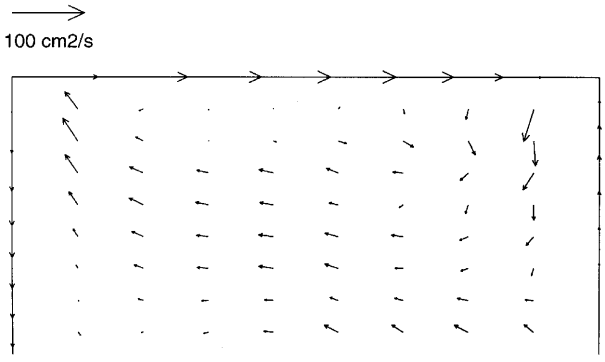

Figure 20. Residual transport of upstream region with Neumann condition on bay

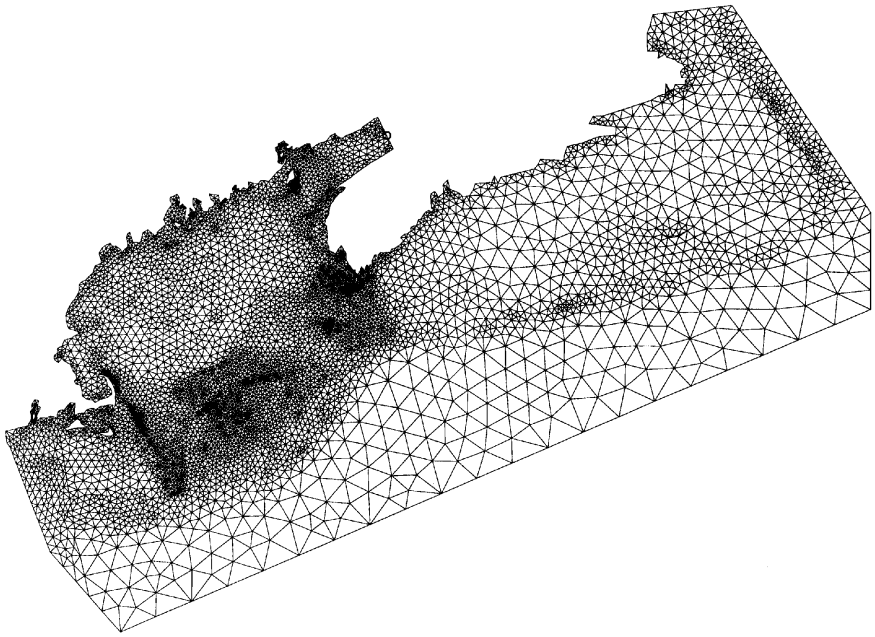

Figure 21. G2S mesh—6756 nodes, 12,877 elements. The circle on the Bay of Fundy boundary is node 6721 in the next figures

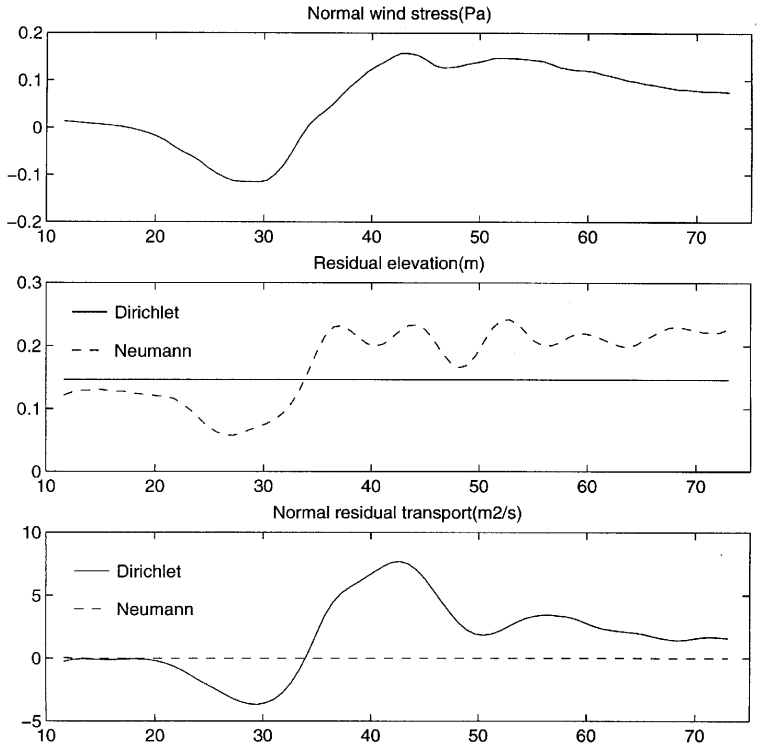

Figure 22. Moving average time series at node 6721. The normal direction convention is positive out of the domain and negative into it. The x-axis is in hours and the averages are plotted at the end of the averaging period

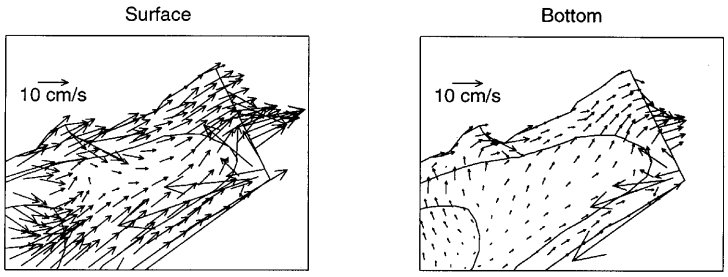

Figure 23. Residual velocity at surface (left) and bottom (right) with Dirichlet condition across cut; $t = 40{\cdot}365$ h

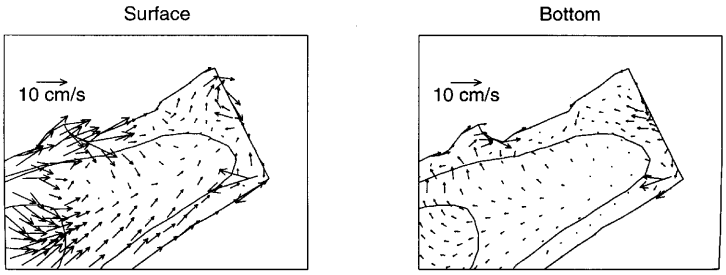

Figure 24. Residual velocity at surface (left) and bottom (right) with Neumann condition across cut; $t = 40{\cdot}365$ h. Note that $\mathbf{v} \cdot \hat{\mathbf{n}}$ is positive (outward) at the surface and negative at depth; its vertical average is zero

ocean instead of the small, bounded bay. However, in the Neumann case it is evident that the circulation feels the presence of the enclosed bay and reacts accordingly with return flow at depth.

7. CONCLUSIONS

There are a few main points.

1. Equations (7), (8) and (24), (27) are global mass balance relations which govern all solutions obtained with the procedures outlined. Solutions initially in balance will remain so; mass imbalance is removed at the rate τ_0.
2. The equivalence of the Neumann and Dirichlet problems guarantees that the mass balance relations pertain in either case, with the participating boundary transports matched to the normal component of the velocity profile on the boundary according to equation (12) or (13).
3. The strong enforcement of normal transport on the 3D velocity solution is done not by discarding momentum balances at the boundary but by correcting the interior pressure gradient there. This fact is obscured in 2D analyses but clear in 3D. Equation (41) defining α is the key relation.
4. The inference of the boundary transport along Dirichlet boundaries is given by equation (43). This discretization requires $\varepsilon > \frac{1}{2}$ for stability.
5. Mass-conserving solutions obtained with these procedures are superior to their 'conventional' predecessors.

ACKNOWLEDGEMENTS

We are grateful for financial support from the USGLOBEC Program, the Gulf of Maine Regional Marine Research Program and the New Hampshire Sea Grant College Program. This is USGLOBEC Contribution number 75.

REFERENCES

1. J. J. Westerink and W. G. Gray, 'Progress in surface water modeling', *Rev. Geophs.*, **29** (April Suppl.), 210–217 (1991).
2. D. R. Lynch, J. T. C. Ip, C. E. Naimie and F. E. Werner, 'Comprehensive coastal circulation model with application to the Gulf of Maine', *Continental Shelf Res.*, **16**, 875–906 (1996).
3. G. F. Carey (ed.), *Finite Element Modeling of Environmental Problems*, Wiley, Chichester, 1995.
4. D. R. Lynch and A. M. Davies (eds), *Quantitative Skill Assessment for Coastal Ocean Models*, CES Vol. 47, American Geophysical Union, Washington, DC, 1995.
5. J. J. Westerink, R. A. Luettich, J. K. Wu and R. L. Kolar, 'The influence of normal flow boundary conditions on spurious modes in finite element solutions to the shallow water equations', *Int. j. numer. methods fluids*, **18**, 1021–1060 (1994).
6. M. T. Johnsen and D. R. Lynch, 'A second-order radiation boundary condition for the shallow water wave equations on two-dimensional unstructured finite element grids', *Int. j. numer. methods fluids*, **18**, 575–604 (1994).
7. M. T. Johnsen and D. R. Lynch, 'Assessment of a second-order radiation boundary condition for tidal and wind-driven flows', in D. R. Lynch and A. M. Davies (eds), *Quantitative Skill Assessment for Coastal Ocean Models*, CES Vol. 47, American Geophysical Union, Washington, DC, 1995, pp. 49–70.
8. R. L. Kolar, W. G. Gray and J. J. Westerink, 'Boundary conditions in shallow water models—an alternative implementation for finite element codes', *Int. j. numer. methods fluids*, **22**, 603–618 (1996).
9. D. R. Lynch and F. E. Werner, 'Three-dimensional hydrodynamics on finite elements. Part I: Linearized harmonic model', *Int. j. numer. methods, fluids*, **7**, 871–909 (1987).
10. D. R. Lynch and F. E. Werner, 'Three-dimensional hydrodynamics on finite elements. Part II: Non-linear time-stepping model', *Int. j. numer. methods fluids*, **12**, 507–533 (1991).
11. D. R. Lynch, F. E. Werner, D. A. Greenberg and J. W. Loder, 'Diagnostic model for baroclinic and wind-driven circulation in shallow seas', *Continental Shelf Res.*, **12**, 37–64 (1992).
12. D. R. Lynch, 'Mass balance in shallow water simulations', *Commun. Appl. Numer. Methods*, **1**, 153–159 (1985).
13. D. R. Lynch, 'Mass conservation in finite element groundwater models', *Adv. Water Resources*, **7**, 67–75 (1984).
14. P. M. Gresho, R. L. Lee, R. L. Sani, M. K. Maslanik and B. E. Eaton, 'The consistent Galerkin FEM for computing derived boundary quantities in thermal and/or fluid problems', *Int. j. numer. methods fluids*, **7**, 371–394 (1987).
15. J. D. Wang and J. J. Connor, 'Mathematical modeling of near coastal circulation', *Tech. Rep. 200*, Ralph M. Parsons Laboratory, MIT, Cambridge, MA, 1975.
16. W. G. Gray, 'On normal flow boundary conditions in finite element codes for two-dimensional shallow water flow', *Int. j. numer. method fluids*, **4**, 99–104 (1984).
17. D. R. Lynch, M. J. Holboke and C. E. Naimie, 'The Maine Coastal Current: spring Climatological circulation', *Continental Shelf Res.*, **17**, 605–634 (1997).
18. D. R. Lynch and Naimie, 'The M2 tide and its residual on the outer banks of the Gulf of Maine', *J. Phys. Oceanogr.*, **23**, 2222–2253 (1993).
19. C. E. Naimie, J. W. Loder and D. R. Lynch, 'Seasonal variation of the three-dimensional residual circulation of Georges Bank', *J. Geophys. Resch.*, **99**, (C8), 15 967–15 989 (1994).
20. M. J. Holboke and D. R. Lynch, 'Simulations of the Maine Coastal Current', *Proc. ASCE 4th Int. Conf. on Estuarine and Coastal Modeling*, San Diego, CA, October 1995, ASCE, New York, 1996

